



OPEN

## Enhancement of dielectric and conductive properties of $\text{Mn}_2\text{O}_3$ nanoparticles in liquid crystal under argon radio frequency plasma

Mahsa Khadem Sadigh<sup>1</sup>✉, M. A. Mohammadi<sup>2</sup>, F. Baharlounezhad<sup>2</sup> & A. Ranjkesh<sup>3</sup>

In this study, the effects of Ar radio plasma on  $\text{Mn}_2\text{O}_3$  nanoparticles and their influence on the permittivity and electrical properties of doped nematic liquid crystal were investigated. The nanoparticles were plasma-treated at different times and then added to the liquid crystal. The size of the nanoparticles and the surface morphology changed with increasing plasma application time. According to the results, significant changes in dielectric anisotropy were observed, the highest value of which was obtained after 2 min of plasma treatment. Also, changes in the parallel and vertical components of the permittivity indicated the effect of the orientation of the nanoparticles and the structure of the liquid crystal under the influence of Ar plasma. The impedance results also showed a significant decrease in impedance and improvement in conductivity of the liquid crystal matrix with increasing plasma treatment time, which was consistent with the equivalent circuit modeling. This study shows that the use of Ar radio plasma can be considered as a method for optimizing the properties of doped liquid crystals with nanoparticles in electronic and optoelectronic applications.

**Keywords** Argon plasma, Anisotropy, Impedance, Liquid crystal, Nanoparticle

Liquid crystals (LCs) are distinctive mesophases exhibiting properties between liquids and solids, enabling wide application in displays, sensors, and adaptive devices<sup>1–5</sup>. Similar to isotropic media, the addition of dyes and nanoparticles (NPs) with different structure and size to anisotropic media such as liquid crystals can improve their optical, electrical and thermal properties. In addition, mechanical methods as applying electric and magnetic fields also play a significant role in increasing the efficiency and performance of liquid crystals<sup>6–11</sup>. In particular, metal-oxide NPs such as  $\text{TiO}_2$ ,  $\text{ZnO}$ , and  $\text{Al}_2\text{O}_3$  have been demonstrated to modify dielectric anisotropy, conductivity, and switching behaviors in LCs. This group of nanoparticles is synthesized by various methods and is widely used in various industries such as oil, gas, and medicine<sup>12,13</sup>. Recent reviews have systematically highlighted the synthesis strategies, nanoparticle-LC interactions, and functional enhancements achieved in nanocomposite LCs, emphasizing the influence of nanoparticle type, size, and surface chemistry. Within this context,  $\text{Mn}_2\text{O}_3$  nanoparticles offer a compelling choice due to their multivalent redox states, oxygen-vacancy-rich surfaces, and tunable nanostructures-attributes that can strongly influence permittivity and impedance properties. Studies have shown that tuning the size of  $\text{Mn}_2\text{O}_3$  NPs their interfacial interaction and dispersion stability when embedded in anisotropic media, crucial for liquid crystal performance<sup>14–22</sup>. The surface condition of nanoparticles is also essential. The combination of plasma and nanotechnology with plasma science led to produce, modify, and functionalize nanostructures with high precision. Application of this combination include the synthesis of nanoparticle and production nanostructured coating with improved mechanical and electronic properties. This technology has wide application in fields such as catalysis, sensors, targeted drug delivery, and modern medicine, and it allows for reduction the activation energy of chemical reactions and increasing of efficiency of nonchemical processes<sup>23–29</sup>. Conventional chemical functionalization often leaves surface residues that disrupt LC alignment. In contrast, plasma treatment provides a clean, residues-free method to modify NP surfaces by introducing controlled functionality (oxygen vacancies, surface charges) while preserving crystallinity. Plasma-treated metal-oxide NPs have shown improved electro-optic behavior in LC hosts compared to chemically synthesized counterparts.

<sup>1</sup>Department of Laser and Optics Engineering, University of Bonab, Bonab, Iran. <sup>2</sup>Faculty of Physics, University of Tabriz, Tabriz, Iran. <sup>3</sup>Condensed Matter Department, J. Stefan Institute, Jamova 39, Ljubljana, Slovenia. ✉email: mahsa.sadigh@ubonab.ac.ir; mahsa.sadigh@yahoo.com

Despite these advances, no studies to date have examined the effects of Ar-plasma treatment on  $\text{Mn}_2\text{O}_3$  within nematic-LCs. Addressing this gap, our work focuses on how Ar-plasma processing of  $\text{Mn}_2\text{O}_3$  influences dielectric anisotropy ( $\Delta\epsilon$ ) and electrical impedance in ML-0648 nematic LC. We expose  $\text{Mn}_2\text{O}_3$  NPs to controlled plasma conditions, then disperse them at 0.5 wt% into the LC, and measure  $\epsilon_{\parallel}$ ,  $\epsilon_{\perp}$ ,  $\Delta\epsilon$ , and impedance (real and imaginary parts) across temperature and frequency. This study aims to demonstrate how plasma engineering of NP surface properties can be harnessed to optimize electro-optic performance in LC-based devices.

## Experimental

### Materials

The study employed ML-0648 nematic liquid crystal and  $\text{Mn}_2\text{O}_3$  nanoparticles, both supplied by Merck. The liquid crystal's nematic to isotropic phase transition temperature, as specified by the manufacturer, is near 81 °C.

### Cell Preparation

In this work, both homotropic and planar liquid crystal cells were fabricated. The construction process involved carefully positioning the samples between two indium tin oxide (ITO) coated optical glass substrates. Surface alignment was established by applying a polyvinyl alcohol (PVA), which was subsequently subjected to unidirectional rubbing to induce the desired molecular orientation (planar alignment). To promote homotropic alignment in the cell lecithin was employed. A Mylar spacer was introduced to ensure a uniform cell gap between the electrode interfaces. Finally, the cell assembly was sealed using an appropriate adhesive to secure the substrates and maintain structural integrity.

### Characterizations

The physicochemical properties of the nanoparticles were systematically characterized using a high-resolution field emission scanning electron microscope (SEM-JSM-7600 F), enabling detailed morphological analysis. Crystallin structure were investigated via X-ray diffraction (XRD) employing a Siemens XRD-D5000 diffractometer, utilizing monochromatic  $\text{Cu K}\alpha$  with a wavelength of  $\lambda = 1.5418 \text{ \AA}$ . Transmission electron microscopy (TEM) was carried out using a Philips EM 208 S instrument operated at 100 kV. In addition, Fourier transform infrared (FTIR) spectroscopy (Tensor 27, Bruker, Germany) was employed at room temperature to investigate the structural characteristics of samples. Electrochemical impedance spectroscopy (EIS) measurements of planar cells were performed using an Ivium Stat. h potentiostat/galvanostat system at the range of 0.1 Hz-0.1 MHz. Permittivity of the nematic liquid crystal systems doped with  $\text{Mn}_2\text{O}_3$  nanoparticles was carried out using a precision LCR meter (VICTOR 4091 C) at the 10 kHz frequency and AC amplitude of 0.3 V, integrated with a temperature-regulated sample chamber with accuracy of  $\pm 0.1$  °C to ensure thermal stability during measurements. 10 kHz was selected below the relaxation regimes because at this frequency the impact of electrode polarization is reduced while the measured permittivity still provides a reliable representation. The LC-nanoparticle hybrid systems were confined Whitin capacitor-type cells, specifically engineered to support both planar and homotropic molecular alignments for comparative permittivity evaluation. Capacitance measurements were conducted as a function of temperature, both in the absence (reference cell) and presence of the doped liquid crystal medium.  $\epsilon_{\parallel}$  and  $\epsilon_{\perp}$  denote the permittivities measured parallel and perpendicular to the nematic director  $\mathbf{n}$ , which is the unit vector describing the average orientation of the molecular long axes<sup>30</sup>. These components were extracted using the following analytical expressions:

$$\epsilon_{\parallel} = \frac{C_{\perp}}{C_0} \quad (1)$$

$$\epsilon_{\perp} = \frac{C_{\parallel}}{C_0} \quad (2)$$

Here,  $C_{\parallel}$  and  $C_{\perp}$  correspond to the measured capacitances when the director of the liquid crystal molecules is aligned parallel and perpendicular to the electrode surfaces, respectively,  $C_0$  denotes the capacitance of the empty reference cell. The reference capacitance ( $C_0$ ) was determined by measuring the empty cell after open/short calibration. Stray capacitances were minimized using short (< 5 cm) shielded coaxial cables and the instrument guard terminal. The dielectric anisotropy ( $\Delta\epsilon$ ), a key parameter indicative of the material's electro-optic responsiveness, was computed using:

$$\Delta\epsilon = \epsilon_{\parallel} - \epsilon_{\perp} \quad (3)$$

### Plasma setup

According to Fig. 1,  $\text{Mn}_2\text{O}_3$  powders were placed in a radio frequency (RF) plasma reactor for studying the plasma effects. The plasma generator (50 W, 13.56 MHz radio frequency) coupled with a turn copper coil with a 2 mm external diameter installed around a reaction chamber as an electrode. This chamber was in the form of a cylindrical glass tube with a length and external diameter of 300 mm and 60 mm, respectively. Plasma was produced and exerted at 0.001 Torr by using vacuum rotary pump. Argon (Ar) was used as the working gas in the RF plasma reactor.

## Results and discussions

### Properties of nanoparticles under influence of ar plasma

In this section, the effects of plasma on  $\text{Mn}_2\text{O}_3$  nanoparticles are investigated using various analyses.

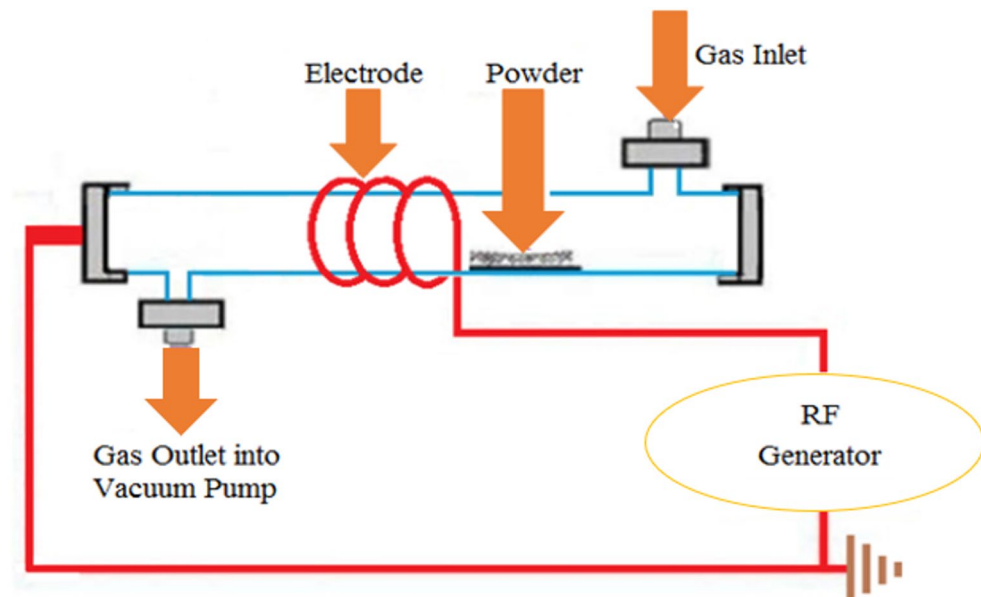


**Fig. 1.** Schematic diagram of the plasma generation and treatment setup.

#### FTIR analysis

The FTIR spectrum (Fig. 2) of the synthesized  $\text{Mn}_2\text{O}_3$  nanoparticles exhibited characteristic absorption bands at 444.32, 531.09, 606.21, and 668.41  $\text{cm}^{-1}$ , which can be attributed to the fundamental stretching and bending vibrations of Mn-O bonds in the crystal lattice. These bands are considered fingerprint peaks of  $\text{Mn}_2\text{O}_3$  and confirm the formation of the manganese oxide phase. Similar assignments of Mn-O stretching vibrations in the range of 500–650  $\text{cm}^{-1}$  have been reported in previous studies<sup>31–33</sup>. A weak band observed at 1120.69  $\text{cm}^{-1}$  may be associated with C-O or C-O-C stretching vibrations originating from organic precursors or surface-bound hydroxyl groups. The absorption band at 1358.83  $\text{cm}^{-1}$  corresponds to symmetric stretching of carbonate species ( $\text{CO}_3^{2-}$ ), most likely due to atmospheric  $\text{CO}_2$  absorption on the nanoparticle surface. The band at 3431.22  $\text{cm}^{-1}$  is attributed to O-H stretching vibrations of surface hydroxyl groups or adsorbed water molecules, while the peak at 1623.39  $\text{cm}^{-1}$  is assigned to H-O-H bending vibrations of molecular water. These bands suggest the presence of physiosorbed moisture and surface hydroxyl functionalities, which are common in metal oxide nanoparticles. Additionally, a weak band at 2369.30  $\text{cm}^{-1}$  can be assigned to the symmetric stretching mode of gaseous  $\text{CO}_2$ , usually originating from atmospheric contamination during FTIR measurement. FTIR spectra of  $\text{Mn}_2\text{O}_3$  nanoparticles subjected to Ar plasma for 2, 7, and 14 min revealed no appearance of new absorption bands or disappearance of the intrinsic Mn-O lattice vibrations (444–668  $\text{cm}^{-1}$ ), confirming the structural stability of the oxide framework. The only notable modification was a progressive reduction in the intensity of the O-H stretching band at 3431  $\text{cm}^{-1}$  and the C-O/C-O-C related band at 1121  $\text{cm}^{-1}$  after 14 min of treatment. The attenuation is attributed to plasma-assisted desorption and sputtering of surface-absorbed water, hydroxyl groups, and residual organic species, indicating the Ar plasma primarily induces surface cleaning rather than bulk structural alteration.

#### XRD

XRD analysis (Fig. 3) revealed that the positions of the diffraction peaks remain unchanged after plasma treatment, confirming that the crystal structure of  $\text{Mn}_2\text{O}_3$  nanoparticles is preserved. However, the peak intensity and width are sensitive to plasma exposure time: the intensities increase for 2 and 14 min but decrease at 7 min, which reflects modifications in crystallinity and surface defect density.

Using the Scherr equation<sup>33,34</sup>, the size of the crystals under plasma showed that initially the size of the nanoparticles was about 31.95 nm. By applying plasma for 2, 7 and 14, respectively, the size of the nanoparticles reached 31.28, 32 and 31.24 nm. Thus, the size of the nanoparticles under the influence of plasma not show a regular trend, it initially decreases and increases with the application of plasma for 7 min and decreases again with the application of plasma for 14 min.

#### Scanning electron microscopy (SEM) analysis

SEM images (Fig. 4) reveal that the morphology of  $\text{Mn}_2\text{O}_3$  nanoparticles is strongly influenced by Ar plasma treatment. In the untreated sample ( $t=0$ ), the particles predominantly appear as large, irregular agglomerates with rough surfaces. After 2 min of plasma exposure, the agglomerates begin to fragment, resulting in smaller and more compact structures with improved homogeneity. Extending the treatment to 7 min leads to secondary growth and partial re-agglomeration of the particles, forming larger, more spherical structures. However, with prolonged treatment up to 14 min, the morphology undergoes a significant transformation toward finer and more uniformly distributed nanoparticles, accompanied by a substantial reduction in agglomeration. These

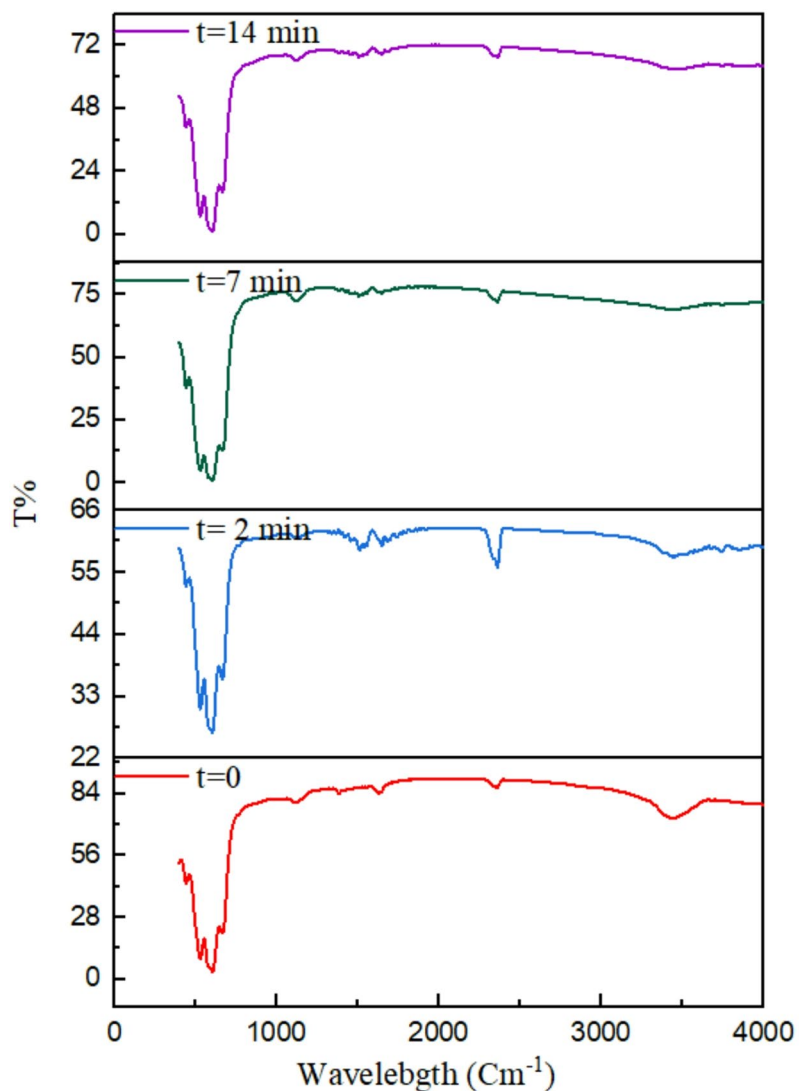


**Fig. 2.** FTIR of liquid crystal samples under influence of Ar plasma at different times.

observations indicate the plasma exposure time plays a critical role in tailoring the particle morphology, with an optimal time it is possible to achieve a uniform and stable nanostructure.

#### *Transmission electron microscopy (TEM) analysis*

TEM analysis (Fig. 5) revealed that the untreated  $\text{Mn}_2\text{O}_3$  nanoparticles were highly agglomerated with an average particle size of about 88 nm. After 2 min of Ar plasma exposure, the agglomerates were effectively broken apart, leading to well-dispersed and more uniform nanoparticles with a reduced average size of 65 nm. Extending the treatment time to 7 min resulted in particle growth up to 75 nm, which can be attributed to localized heating that promotes surface diffusion and particle sintering. At 14 min, the average size slightly decreased to 70 nm, likely due to the competing effects of sputtering and re-agglomeration. Overall, the results indicate that short plasma treatment improves dispersion and reduces particle size, while prolonged exposure favors coalescence and growth. The discrepancy between the particle sizes obtained from XRD (using Scherrer equation) and TEM analysis is mainly attributed to the fact that these two techniques probe different structural features. XRD provides the average crystallite size, which corresponds to coherently diffracting domains within the nanoparticles. In contrast, TEM directly visualizes the overall particle size, which may include multiple crystallites, amorphous surface layers, or agglomerated structures. Furthermore, peak broadening in XRD can also arise from lattice strain and crystal defects, leading to an underestimation of crystallite size. Therefore, the larger values, observed in TEM compared to XRD are expected and reflect the distinction between crystallite size and actual particle or agglomerate dimensions.

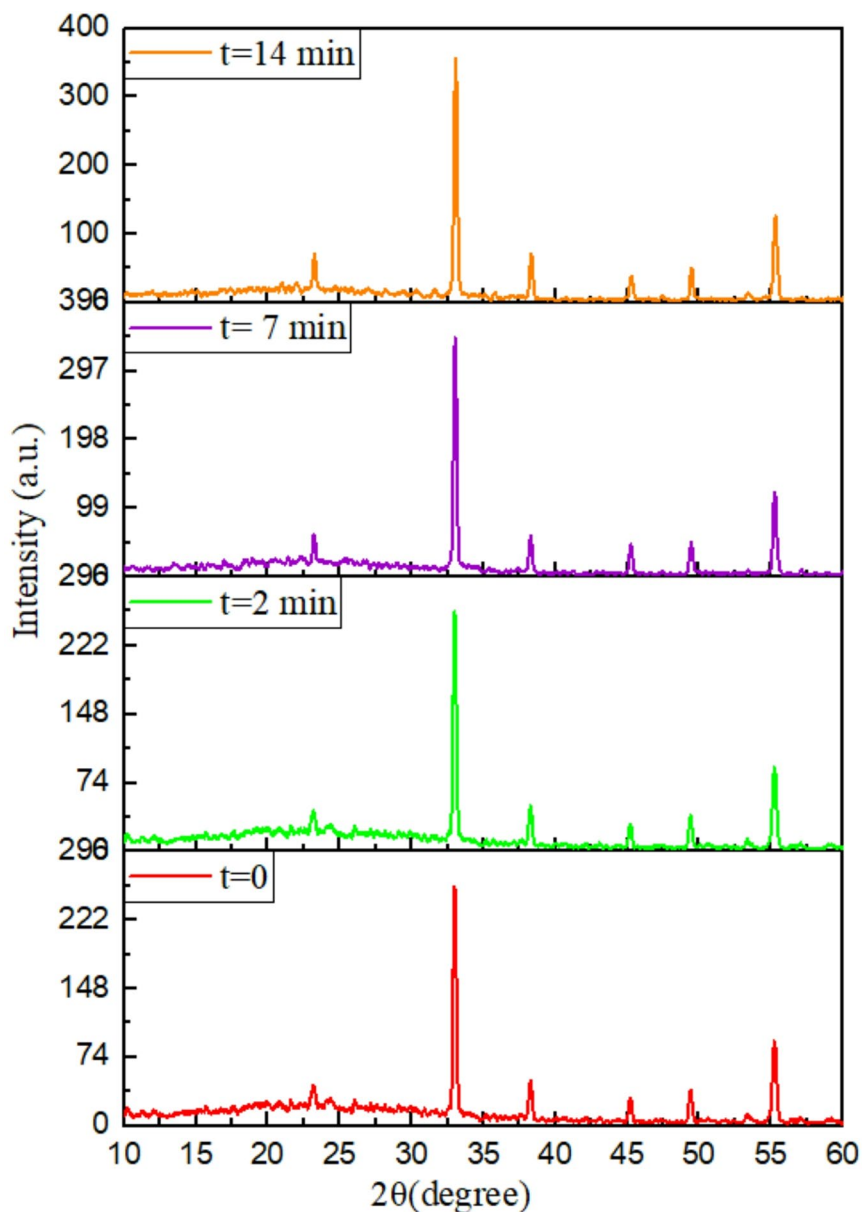


**Fig. 3.** X-ray diffraction (XRD) patterns illustrating structural modifications in liquid crystal samples after exposure to argon plasma for different time intervals.

#### Temperature-dependent permittivity and dielectric anisotropy under the influence of ar plasma

According to Fig. 6, the parallel ( $\epsilon_{\parallel}$ ) and perpendicular ( $\epsilon_{\perp}$ ) components of the permittivity of  $\text{Mn}_2\text{O}_3$  doped liquid crystal samples exhibit distinct temperature-dependent behavior. Across the entire temperature range,  $\epsilon_{\parallel}$  remains consistently higher than  $\epsilon_{\perp}$  highlighting the dominant polarizability along the molecular long axis and its key contribution to dielectric anisotropy. With increasing temperature,  $\epsilon_{\parallel}$  initially rises due to enhanced molecular mobility and longitudinal polarizability, then decreases near the nematic-to-isotropic transition and finally stabilizes in the isotropic phase. Conversely,  $\epsilon_{\perp}$  exhibits the opposite trend. The temperature dependence of the perpendicular permittivity ( $\epsilon_{\perp}$ ) can be attributed to dipolar correlations. As temperature increases, reduced orientational order weakens cooperative dipolar interactions, causing an initial decrease in  $\epsilon_{\perp}$ . Near the nematic-to-isotropic transition, molecular reorientations become less constrained, leading to a slight increase before reaching a constant value in the isotropic phase. The 2-minute plasma-treated sample exhibits the highest  $\epsilon_{\parallel}$  at low temperatures and the largest difference from  $\epsilon_{\perp}$ , while longer plasma treatments modify nanoparticle dispersion and surface structure, reducing the parallel component and slightly enhancing the perpendicular component. In general, this behavior at 2 min is attributed to the increased molecular mobility at elevated temperatures, which allows the longer plasma-induced surface modifications and improved nanoparticle dispersion to maximize the polarizability along the molecular long axis. Therefore, the difference in  $\epsilon_{\parallel}$  enhancement between low and high

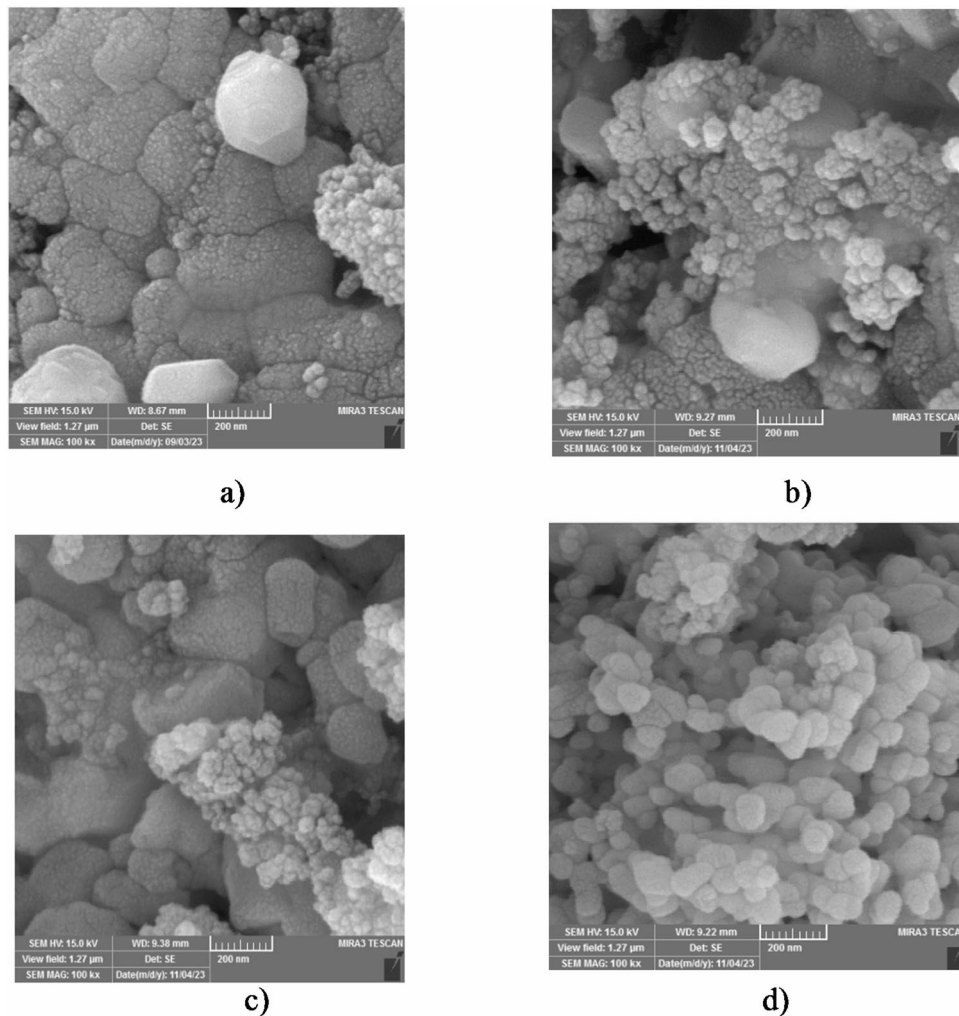


**Fig. 4.** Scanning electron microscopy (SEM) micrographs of liquid crystal samples treated with argon plasma at (a)  $t=0$  min, (b)  $t=2$  min, (c)  $t=7$  min, and (d)  $t=14$  min, showing morphological evolution over time.

temperatures arises from the combined effects of surface modification and temperature-dependent molecular mobility.

The experimental results (Fig. 7) indicate that dielectric anisotropy ( $\Delta\epsilon$ ) reaches its maximum for the 2-minutes plasma sample, followed by the 14-minute, 7-minute, untreated nanoparticles, and pristine liquid crystal. This trend aligns with the enhanced local polarizability and reduced energy barrier for molecular reorientation observed in the short plasma exposure, whereas longer treatments partially mitigate these effects due to surface restructuring and minor aggregation. XRD analysis (Fig. 4) revealed that the positions of the diffraction peaks remain unchanged after plasma treatment, confirming that the crystal structure of  $\text{Mn}_2\text{O}_3$  nanoparticles is preserved. However, the peak intensity and width are sensitive to plasma exposure time: the intensities increase for 2 and 14 min but decrease at 7 min, which reflects modifications in crystallinity and surface defect density. SEM (Fig. 5) images further show that the average particle size initially decreases upon 2-minutes plasma treatment, increases slightly at 7 min, and then decreases again after 14 min. The non-monotonic trend suggests that short plasma exposure removes surface impurities and activates nanoparticle surfaces, leading to improved dispersion and reduced size, while longer exposure (7 min) promotes partial aggregation, increasing the apparent size. At 14 min, further plasma-induced etching and surface restricting dominate, resulting in reduced size and enhanced surface activation. These structural and morphological evolution are consistent with the permittivity results, as short plasma exposure enhances order and polarizability, whereas prolonged treatment introduces competing of aggregation and surface modification, which modulate both dielectric anisotropy and activation energy.

The frequency-dependent permittivity of  $\text{Mn}_2\text{O}_3$ -doped liquid crystal samples (Fig. 8) exhibits distinct behaviors in low-and high-frequency regions, strongly influenced by Ar plasma treatment time. At low frequencies,  $\epsilon$  decreases with increasing frequency, with the highest values observed for the 14 min plasma-treated sample, followed by 2 min, 7 min, untreated, and pure LC. At higher frequencies,  $\epsilon$  approaches a constant value, with the maximum observed for the 2 min plasma-treated sample. The loss spectra also decrease with frequency and asymptotically approach zero. This behavior is consistent with our structural analyses (XRD, SEM,

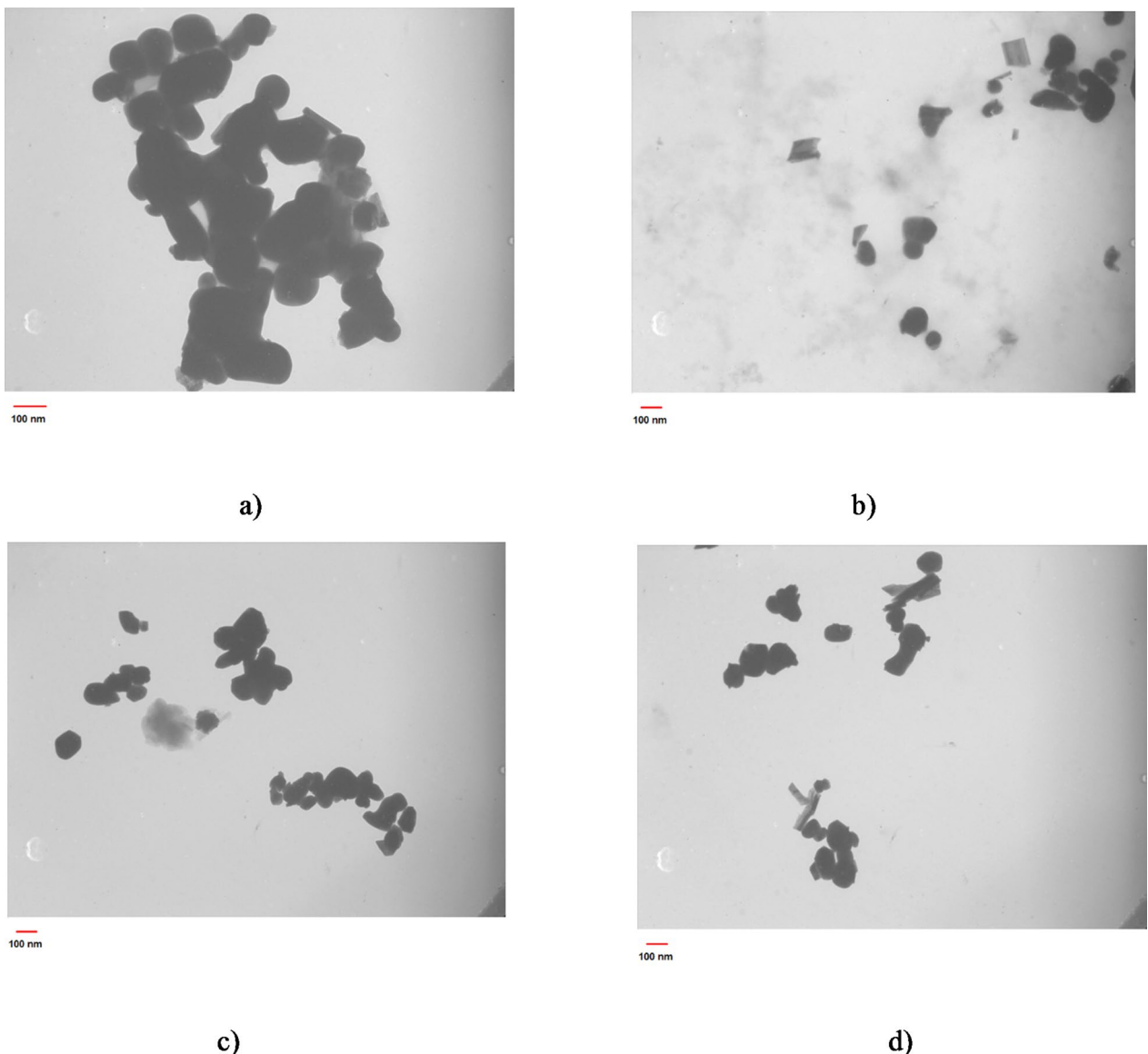


**Fig. 5.** TEM images of (a)  $\text{Mn}_2\text{O}_3$  nanoparticles without plasma treatment, (b)  $\text{Mn}_2\text{O}_3$  under influence of plasma for  $t = 2$  min, (c)  $\text{Mn}_2\text{O}_3$  under influence of plasma for  $t = 7$  min, (d)  $\text{Mn}_2\text{O}_3$  under influence of plasma for  $t = 14$  min.

TEM): short plasma treatment (2 min) improves nanoparticle dispersion and enhances interfacial polarization at high frequencies, whereas prolonged exposure (14 min) favors interfacial polarization at low frequencies due to partial aggregation and surface restricting. These results confirm that plasma-induced surface modifications govern the dielectric response across the entire frequency spectrum.

Moreover, Activation energies ( $E_a$ ) were exacted from nonlinear fitting of  $\Delta\epsilon(T)$  to the Vogel-Fulcher-Tamman model<sup>35</sup>. The activation energy values found to be 143.58 kJ/mol for the pure LC, 129.93 kJ/mol for the liquid crystal doped with  $\text{Mn}_2\text{O}_3$  nanoparticles, 83.831 kJ/mol for the nanoparticle sample treated with argon plasma for 2 min, 108.95 kJ/mol for the plasma treatment of 7 min, and 88.90 kJ/mol for the plasma treatment of 14 min. The 2-minute plasma sample exhibits the lowest  $E_a$ , indicating facilitated molecular reorientation and enhanced local order along the molecular axis. Longer plasma treatments (7 and 14 min) increase  $E_a$  to the 2-minute sample, reflecting modifications in nanoparticle samples show the highest activation barriers. Overall, short-duration plasma treatment optimizes nanoparticle dispersion and surface activation, maximizing molecular dynamics and dielectric anisotropy, whereas prolonged plasma exposure partially diminishes these effects.

The obtained results demonstrate that the variations in permittivity components, anisotropy, and activation energy are directly governed by the order parameter and molecular interactions in the presence of  $\text{Mn}_2\text{O}_3$  nanoparticles and their plasma-induced surface modification. With increasing temperature, the order parameter decreases, leading to a reduction in long-range molecular alignment. Consequently, the parallel component,

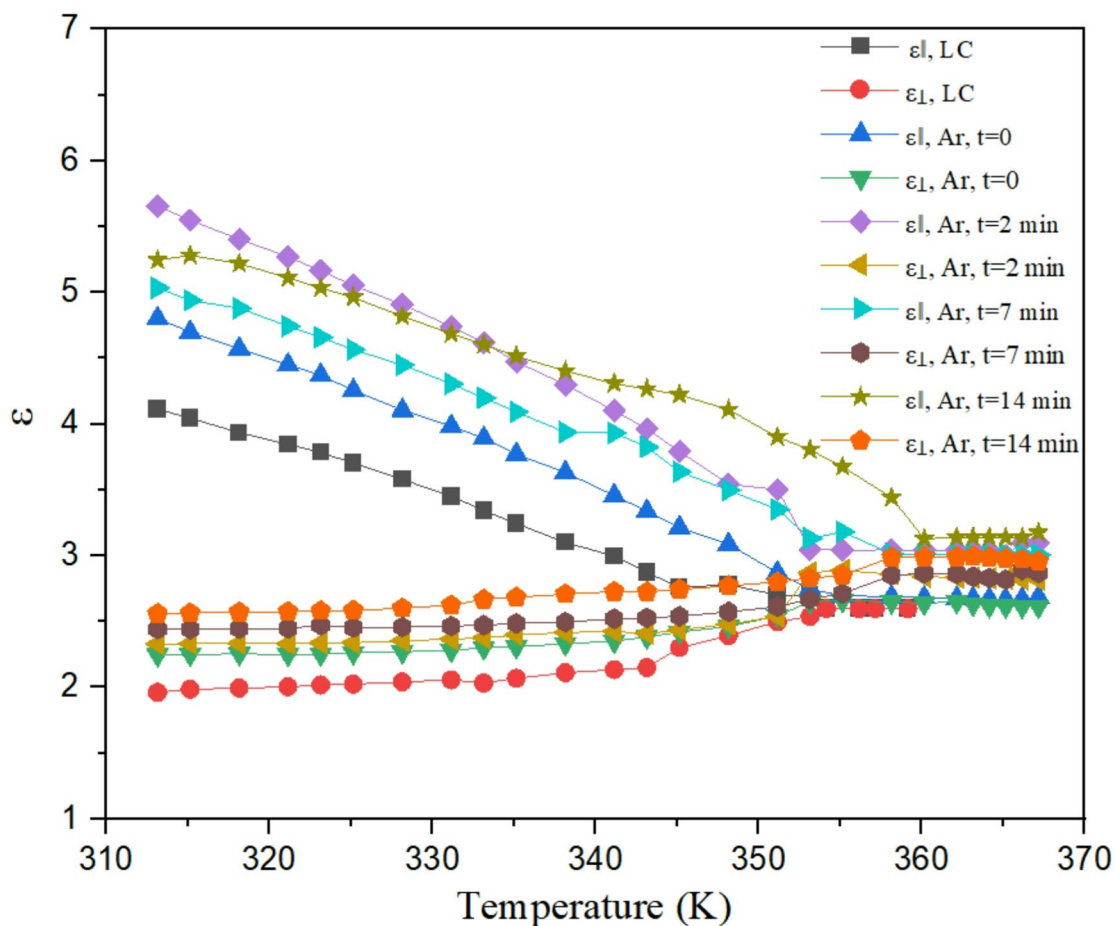


**Fig. 6.** Temperature dependence of the parallel ( $\epsilon_{\parallel}$ ) and perpendicular ( $\epsilon_{\perp}$ ) components of the permittivity of liquid crystal samples subjected to argon plasma treatment at varying exposure durations.

which reflects polarizability along the molecular long axis, exhibits higher values at lower temperatures but decrease as the nematic-isotropic transition is approached. The incorporation of nanoparticles, particularly with short plasma treatment (2 min), enhances intermolecular interactions and improves nanoparticle dispersion within the matrix, thereby maximizing parallel polarizability and dielectric anisotropy. Under these conditions, the activation energy decreases, indicating facilitated molecular orientation and reduction of the energetic barriers for dipolar motion. However, with prolonged plasma exposure (7 and 14 min), surface restructuring and partial aggregation of nanoparticles reduce the degree of uniform interactions, diminishing positive effect observed at short treatment, which in turn increases or stabilizes the activation energy at intermediate values. In addition, the inclusion of nanoparticles and plasma treatment shifts the nematic-isotropic transition temperature to higher values. This effect arises from stronger coupling between the host molecules and plasma-activated nanoparticles, which increases the order parameter and stabilizes the nematic phase, thereby requiring thermal energy to disrupt the molecular order and induce the isotropic state.

In most earlier studies (Table 1) in oxide nanoparticle-LC composites, the dielectric anisotropy was primarily controlled by varying the nanoparticle concentration. For example, ZnO, TiO<sub>2</sub>, and Fe<sub>2</sub>O<sub>3</sub> nanoparticles enhanced  $\Delta\epsilon$  as their loading increased, whereas CuO and MgO showed concentration-dependent reductions or non-monotonic behavior. These trends confirm that the extent of dielectric anisotropy in conventional nanocomposites is strongly dependent on dopant concentration and dispersion quality. In contrast, the present work demonstrates a distinct approach: by applying argon plasma treatment to Mn<sub>2</sub>O<sub>3</sub> nanoparticles,  $\Delta\epsilon$  can be effectively tuned within a defined time window, even at fixed nanoparticle concentration. The results reveal that plasma activation modifies the nanoparticle surface chemistry, thereby strengthening nanoparticle-LC interactions and enabling control over dielectric anisotropy beyond simple concentration effects. This highlights the novelty present study, where  $\Delta\epsilon$  tuning is achieved through plasma processing rather than concentration variation, offering a new strategy for engineering permittivity in LC-nanoparticle systems.

#### Impedance spectroscopy study under the influence of ar plasma

As shown in Fig. 9, both the real and imaginary parts of the impedance were measured at different frequencies of the applied Ac electric field using the spectroscopic impedance technique. According to Fig. 9, the changes in the real and imaginary parts of the impedance the impedance depend on the applied frequency and duration of Ar

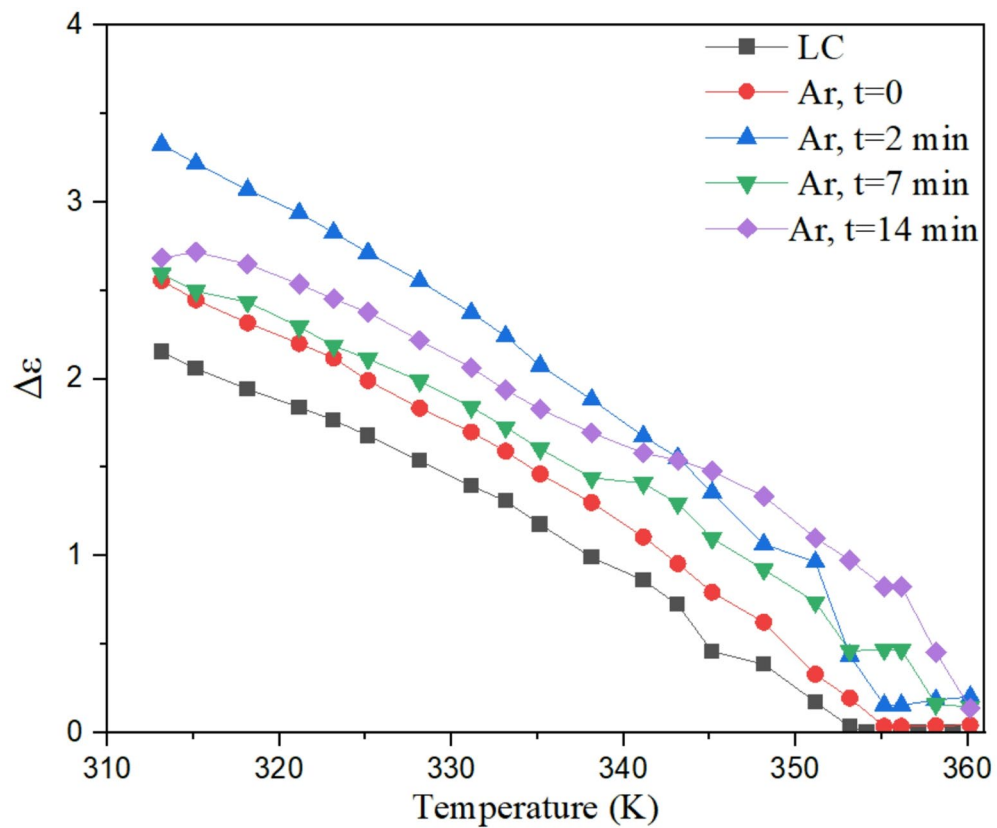


**Fig. 7.** Variation of dielectric anisotropy ( $\Delta\epsilon$ ) as a function of temperature for liquid crystal samples under argon plasma irradiation at multiple exposure times.

plasma application on the doped nanoparticle in the nematic liquid crystal under study. A comparison between the results obtained from impedance spectroscopy for the sample without plasma effects versus the sample caused by Ar plasma shows that plasma effects lead to spectral shifts. Despite the spectral shift, a similar trend of changes with frequency changes was observed in all liquid crystal samples. The real part values of impedance of liquid crystal samples containing  $Mn_2O_3$  nanoparticles gradually decrease with increasing frequency and finally asymptotically approach the horizontal axis. Although a relatively regular behavior was observed in the changes in the real part values, no such behavior was observed in the imaginary part. With increasing frequency, the values of the imaginary part of the impedance of the samples initially show an increasing trend, then a decreasing trend, and finally reach a constant value with increasing frequency. In this case, as the duration of argon plasma application increases, the values of the real and imaginary parts of the impedance gradually decrease. These changes at low frequencies can be caused by the interaction between liquid crystal molecules at the interface with the electric field, and at high frequencies by the interaction of the dipole moment in the bulk state with the electric field<sup>36</sup>. Furthermore, by plotting the values of imaginary part of the impedance in terms of the values of the real part, we can obtain the Cole-Cole curves (Fig. 10). In order to simulate the behavior of liquid crystal samples containing nanoparticles, an equivalent electrical circuit is constructed as shown in Fig. 10, which consist of six components as follows:

$R_{CR}$ : Indicates the specific resistance of external elements and electrode connections.

$R_{LC}$ : Indicates the resistance of the bulk liquid crystal.

$C_{LC}$ : Indicates the capacitance of the bulk liquid crystal.

$C_{DL}$ : Double layer polarity caused by the accumulation of charges near the electrodes.

$W$ : Representation of the Warburg element to describe the drift of charged species in a doped liquid crystal system.

In general, the Cole-Cole plots of the LC- $Mn_2O_3$  samples exhibit a semicircle frequency and an inclined line at low frequencies. The high-frequency semicircle arises from the parallel combination of the bulk liquid crystal resistance and capacitance, representing fast charge transfer processes within the active material. The plot starts from the origin at the left-hand side because, at very high frequencies, the capacitive impedance of the bulk approaches zero, and the system behaves predominantly as the series resistance of the electrodes and connectors; minor deviations from ideality can be attributed to parasitic effects. The low-frequency inclined line corresponds to the Warburg element in parallel with double-layer capacitance, reflecting diffusion-limited ionic transport at the electrode-electrolyte interface. This behavior is fully consistent with the proposed equivalent circuit comprising the series resistance of the electrodes and connectors, the parallel bulk resistance and capacitance,

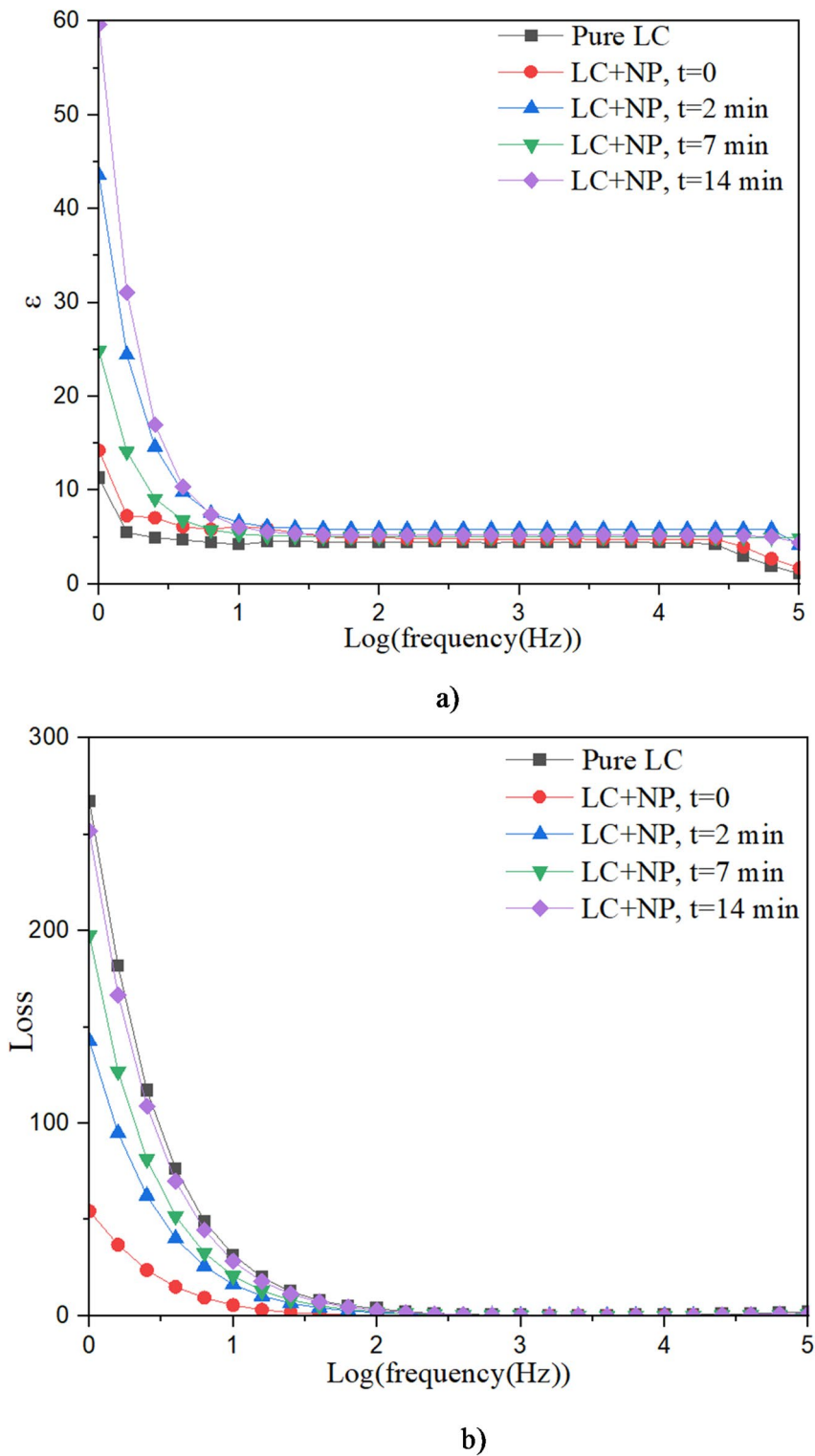


**Fig. 8.** The curves of (a) permittivity and (b) loss as a function of frequency for planar liquid crystal cell.

and, in series, the parallel combination of double-layer capacitance and Warburg impedance, and aligns with previously reported results<sup>37,38</sup>.

According to the simulation with the equivalent circuit, the diameter and the edge of the semicircle of the Cole-Cole curves represent  $R_{LC}$  and  $R_{CR}$ , respectively. The straight line in the diagrams is also related to the changes of the parallel set  $W$  and  $C_{DL}$ . As can be clearly seen in Fig. 10, the symbols represent the experimental data and the solid curves represent the results obtained from the fitting based on the equivalent circuit. The values obtained for the best fit (with an error of less than 5%) are shown in Table 1. The resistance values

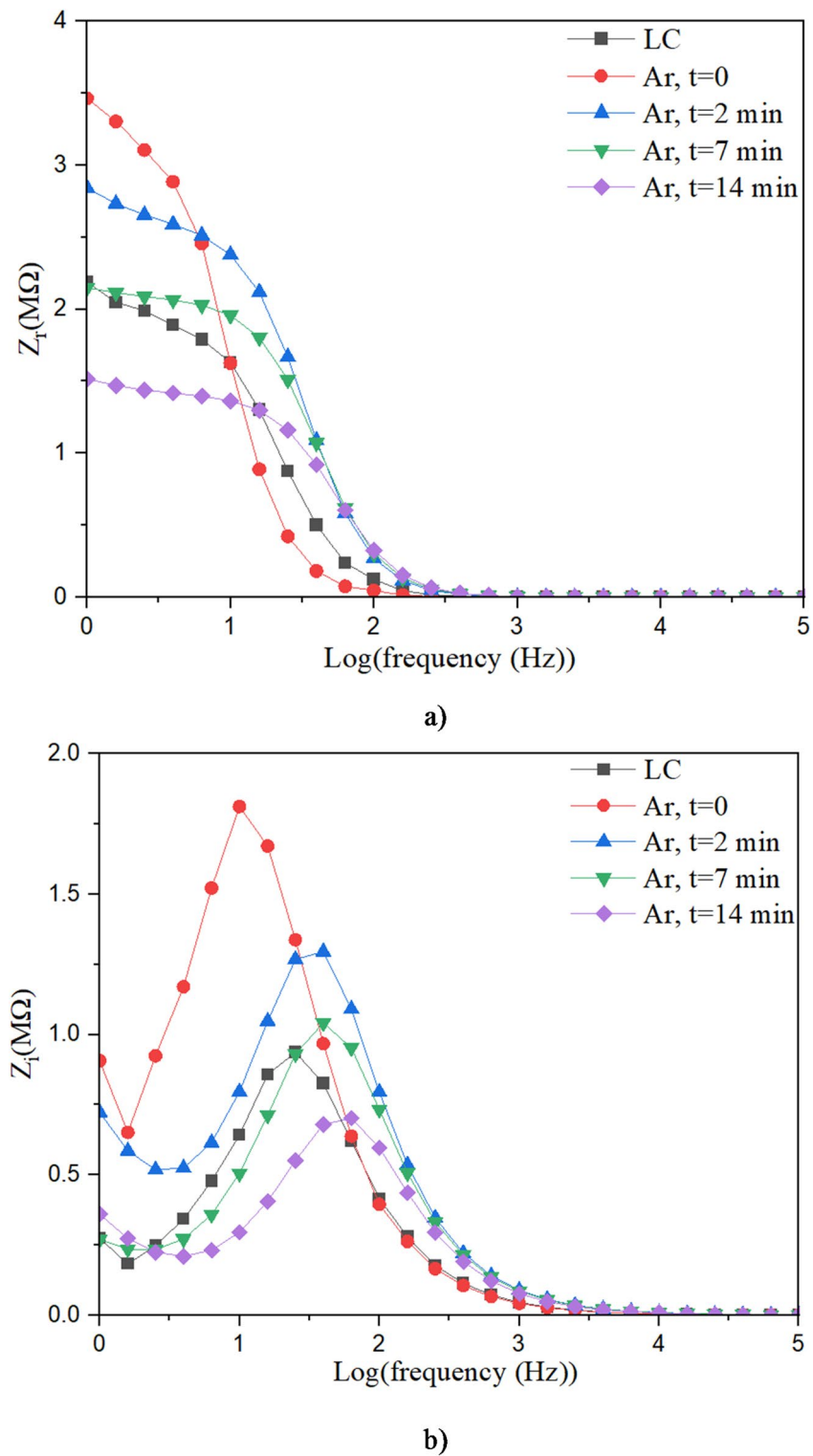


**Fig. 9.** Frequency-dependent changes in the real and imaginary components of the impedance of liquid crystal samples exposed to argon plasma at different time intervals.

due to electrodes and connectors are almost constant as expected. According to the data in Table 2, just as the diameter of the Cole-Cole curves decrease with increasing plasma application time in the samples under plasma, the  $R_{LC}$  values also decrease with increasing Ar plasma application time. The results obtained show that by applying plasma to nanoparticles, the conductivity of the liquid crystal matrix increases. In addition, the capacitance of the liquid crystal matrix containing  $Mn_2O_3$  nanoparticles increases with the application of Ar plasma compared to the case without plasma effects. The highest value is related to the time of 14 min, which is

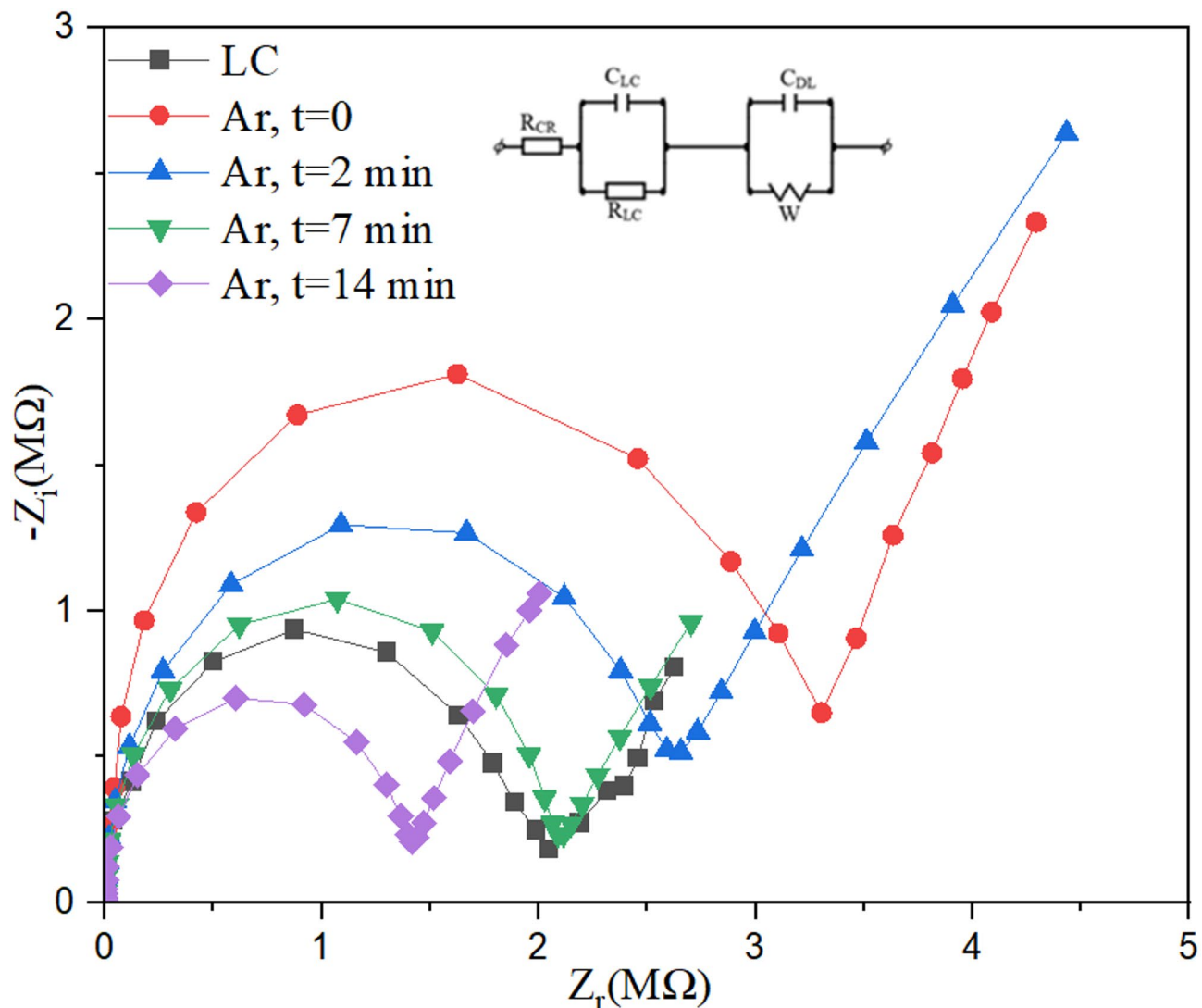


**Fig. 10.** Cole-Cole impedance plots of liquid crystal samples after argon plasma treatment for various durations.

Study	Nanoparticle	LC Host	Parameters/conditions	Effect on $\epsilon$	Effect on $\Delta\epsilon$
Enhancement of dielectric and conductive properties of $Mn_2O_3$ nanoparticles in liquid crystal under argon radio frequency plasma (This work)	$Mn_2O_3$ Plasma treated (2–14 min)	ML-0648	Plasma treatment time (2 min)	$\epsilon$ increases with plasma treatment	$\Delta\epsilon$ significantly enhanced (max at 2 min plasma)
Effect of $\gamma$ - $Fe_2O_3$ nanoparticles on morphological, electro-optical and dielectric properties	$\gamma$ - $Fe_2O_3$ (0–0.05 wt%)	6CHBT	Concentration	$\epsilon$ increases	$\Delta\epsilon$ increases, improving electro-optical properties
Dielectric and electrical properties of nematic LC-6CB doped with $\gamma$ - $Fe_2O_3$	$\gamma$ - $Fe_2O_3$	6CB	Concentration Cell gap	$\epsilon$ strongly dependent on cell thickness	–
Semiconducting CuO nanoparticles in nematic 5CB	CuO	5CB	Concentration	$\epsilon$ decreases	$\Delta\epsilon$ decreases
TiO <sub>2</sub> , ZnO and MB doping in 8CB nematic	TiO <sub>2</sub> , ZnO	8CB	Concentration	$\epsilon$ increases	$\Delta\epsilon$ increases
Ferric Oxide ( $Fe_2O_3$ ) in 8OCB nematic for displays	$Fe_2O_3$ (0–1wt%)	8CB	Concentration	$\epsilon$ increases	$\Delta\epsilon$ increases
MgO nanoparticles in nematic LC	MgO (0–0.6 wt%)	5CB	Concentration	$\epsilon$ increases	$\Delta\epsilon$ Variable

**Table 1.** Comparative studies on permittivity of nematic LCs doped with metal oxide nanoparticles<sup>14–22</sup>.

Sample	$R_{LC}$ (MΩ)	$C_{LC}$ (nF)	$C_{DL}$ (μF)	$W_{sr}$ (MΩs <sup>-0.5</sup> )
LC	1.91	3.18	4.86	0.53
LC + Mn <sub>2</sub> O <sub>3</sub>	3.16	1.44	0.03	6.63
LC + Mn <sub>2</sub> O <sub>3</sub> t = 2 min	2.46	1.86	0.05	5.27
LC + Mn <sub>2</sub> O <sub>3</sub> t = 7 min	2.06	1.87	0.37	6.43
LC + Mn <sub>2</sub> O <sub>3</sub> t = 14 min	1.39	2.14	0.24	3.57

**Table 2.** Extracted equivalent circuit parameters obtained by fitting the impedance spectroscopy data of Mn<sub>2</sub>O<sub>3</sub> nanoparticle-doped liquid crystal samples subjected to argon plasma treatment.

proportional to the change in the values of the vertical component of permittivity with the application of plasma. The changes can be due to the interactions between liquid crystal molecules and nanoparticles, which change with the application of plasma effects. The values obtained for the double layer capacitance also increase with the application of plasma, which can be related to the different effects of plasma on the size nanoparticles and surface morphology at different application times. These results show that the magnitude of capacity at the interface at low frequencies is larger than the capacity of liquid crystal in the bulk. The irregular changes in the W values can be due to molecular interactions with different intensities in the presence and absence of plasma effects. The series resistance  $R_{CR}$ , representing resistance of electrode contacts and connections, is small (~ 80–90 Ω) relative to  $R_{LC}$  (1–3 MΩ) and therefore negligible in the analysis. The overall quality of the fitting (error < 5%) confirms that the equivalent circuit reliably separates bulk, interfacial, and diffusion contributions, demonstrating that the observed changes in impedance upon plasma treatment are primarily due to modifications in  $R_{LC}$ ,  $C_{LC}$ ,  $C_{DL}$ , and W rather than the electrode/contact resistance.

As evidenced by equivalent circuit analysis (Table 2), increasing the plasma treatment time leads to a decrease in the resistance of the liquid crystal layer ( $R_{LC}$ ) and a simultaneous increase in the double-layer capacitance ( $C_{DL}$ ). This behavior indicated that plasma treatment removes surface impurities and ionic centers from Mn<sub>2</sub>O<sub>3</sub> nanoparticles, thereby improving their dispersion and interfacial interactions within the liquid crystal host. Consequently, the ionic contribution to the permittivity diminishes, while the capacitive polarization becomes more dominant. The trend, observed in Fig. 10, is consistent with the previous findings. From an application point of view, such a reduction in ionic effects can be considered a beneficial aspect of plasma treatment, as it enhances electrical stability and improves permittivity values in nanoparticle-doped liquid crystals.

## Conclusions

In this study, permittivity, and structural characteristics of Mn<sub>2</sub>O<sub>3</sub> doped nematic liquid crystals under varying Ar plasma treatments were systematically investigated. The parallel ( $\epsilon_{\parallel}$ ) component of permittivity consistently exceeds the perpendicular ( $\epsilon_{\perp}$ ) component across all temperatures, resulting in enhanced dielectric anisotropy, which is maximized for short plasma exposure (2 min) due to optimal nanoparticle dispersion and surface activation. Frequency-dependent measurements of permittivity reveal that low-frequency interfacial polarization dominates, whereas dipolar orientational polarization governs the intermediate frequency range, both modulated by plasma-induced surface and structural changes. Nonlinear fitting of the dielectric anisotropy with Volgel-Fulcher-Tamman model shows that short plasma treatment significantly reduces the activation energy ( $E_a$ ), facilitating molecular reorientation, whereas longer plasma durations partially restore the energetic barrier due to surface restructuring and nanoparticle aggregation. XRD results confirm that the crystal structure remains unchanged while vary with plasma duration, and SEM images show non-monotonic changes in particle size, reflecting plasma-induced etching and aggregation effects. Impedance spectroscopy and equivalent circuit analysis further demonstrate that plasma treatment decreases bulk resistance and enhances both bulk and interfacial capacitances, indicating improved charge transport, molecular alignment, and electrical stability. Overall, controlled Ar plasma treatment provides a versatile strategy to tune nanoparticle dispersion, surface activation, molecular dynamics, and permittivity values, highlighting its potential for optimizing electro-optical performance in nanoparticle-doped nematic liquid crystals.

## Data availability

Data is provided within the manuscript file.

Received: 2 August 2025; Accepted: 16 October 2025

Published online: 07 November 2025

## References

1. khadem Sadigh, M., Ranjkesh, A. & Hayatifar, B. Improving the nonlinear electro-optical responses of doped nematic liquid crystals with chiral dopants. *Opt. Mater.* **135**, 113352. <https://doi.org/10.1016/j.optmat.2022.113352> (2023).
2. Khadem Sadigh, M., Naziri, P., Ranjkesh, A. & Zakerhamidi, M. S. Relationship of pitch length of cholesteric liquid crystals with order parameter and normalized polarizability. *Opt. Mater.* **119**, 111373. <https://doi.org/10.1016/j.optmat.2021.111373> (2021).
3. Khadem Sadigh, M., Zakerhamidi, M. S. & Ranjkesh, A. Enhanced electro-optical nonlinear responses of doped nematic liquid crystals: towards optoelectrical devices. *Opt. Lasers Eng.* **159**, 107229. <https://doi.org/10.1016/j.optlaseng.2022.107229> (2022).

4. Shen, W. & Guoqiang, L. Recent progress in liquid crystal-based smart windows: Materials, structures, and design. *Laser Photonics Rev.* **17**, 2200207. <https://doi.org/10.1002/lpor.202200207> (2023).
5. Uchida, J., Soberats, B., Gupta, M. & Kato, T. Advanced functional liquid crystals. *Adv. Mater.* **34**, 2109063. <https://doi.org/10.1002/adma.202109063> (2022).
6. Khadem Sadigh, M., Sayyar, Z., Shamkhali, A. N., Teimuri-Mofrad, R. & Rahimpour, K. Investigation of linear and microscopic nonlinear optical responses of 1-indanone compounds in different environments based on Polarity models. *Sci. Rep.* **14**, 26559. <https://doi.org/10.1038/s41598-024-78194-9> (2024).
7. Khadem Sadigh, M., Zakerhamidi, M. S. & Shamkhali, A. N. Contribution of environment Polarity effects on the nonlinear hyperpolarizability and linear optical characteristics of some phenothiazines. *J. Mol. Liq.* **336**, 116328. <https://doi.org/10.1016/j.molliq.2021.116328> (2021).
8. Shen, W., Zhang, H., Miao, Z. & Ye, Z. Recent progress in functional dye-doped liquid crystal devices. *Adv. Funct. Mater.* **33**, 2210664. <https://doi.org/10.1002/adfm.202210664> (2023).
9. Mandal, D. et al. Dispersion of multiferroic nanoparticles in a bent-core nematic liquid crystal: experimental and theoretical study. *J. Mol. Liq.* **430**, 127624. <https://doi.org/10.1016/j.molliq.2025.127624> (2025).
10. Tiwari, S. et al. Impact of diamond nanoparticles on the dielectric and electro-optical properties of nematic liquid crystal. *J. Phys. Chem. Solids.* **203**, 112696. <https://doi.org/10.1016/j.jpcs.2025.112696> (2025).
11. Mhatre, M. M., Katariya-Jain, A., Saeed, M. H. & Deshmukh, R. R. Effects of multifunctional thiol monomers and BaTiO<sub>3</sub> nanoparticles on electro-optical and dielectric properties of polymer dispersed liquid crystal films. *J. Mol. Liq.* **413**, 125945. <https://doi.org/10.1016/j.molliq.2024.125945> (2024).
12. Khalil, M., Jan, B. M., Tong, C. W. & Berawi, M. A. Advanced nanomaterials in oil and gas industry: design, application and challenges. *Appl. Energy.* **191**, 287. <https://doi.org/10.1016/j.apenergy.2017.01.074> (2017).
13. Naseem, T. & Durrani, T. The role of some important metal oxide nanoparticles for Wastewater and antibacterial applications: A review. *J. Environ. Chem. Ecotoxicol.* **3**, 59. <https://doi.org/10.1016/j.jeneco.2020.12.001> (2021).
14. Prakash, J., Khan, S., Chauhan, S. & Biradar, A. M. Metal oxide-nanoparticles and liquid crystal: A review of recent progress. *J. Mol. Liq.* **297**, 112052. <https://doi.org/10.1016/j.molliq.2019.112052> (2020).
15. Montes-Campos, H. et al. Ionic liquids nanoconfined in zeolite-templated carbon: A computational study. *J. Mol. Liq.* **318**, 114264. <https://doi.org/10.1016/j.molliq.2020.114264> (2020).
16. Chemingui, M., Singh, U. B., Yadav, N., Dabrowski, R. S. & Dhar, R. Effect of iron oxide ( $\gamma$ -Fe<sub>2</sub>O<sub>3</sub>) nanoparticles on the morphological, electro-optical and dielectric properties of a nematic liquid crystalline material. *J. Mol. Liq.* **319**, 114299. <https://doi.org/10.1016/j.molliq.2020.114299> (2020).
17. Kovalchuk, O. V. et al. *J. Mol. Liq.* **366**, 1120305. <https://doi.org/10.1016/j.molliq.2022.120305> (2022).
18. Jaiswal, M. et al. Synthesis and characterization of semiconducting copper oxide nanoparticles and their impact on the physical properties of a nematic liquid crystalline material 4-pentyl-4'-cyanobiphenyl. *J. Mol. Liq.* **383**, 122032. <https://doi.org/10.1016/j.molliq.2023.122032> (2023).
19. Ocaya, R. O. et al. Impact of TiO<sub>2</sub>, ZnO, and methylene blue doping on the dielectric anisotropy of planar 8CB nematic liquid crystal. *Opt. Mater.* **150**, 115320. <https://doi.org/10.1016/j.optmat.2024.115320> (2024).
20. Mishra, M., Uttam, R., Dhar, R. & Dabrowski, R. S. Incorporation of magnesium oxide nanoparticles in to nematic liquid crystalline matrix. *Mol. Cryst. Liquid Cryst.* **78**, 26–38. <https://doi.org/10.1080/15421406.2020.1810959> (2020).
21. Chen, C-H. & Dierking, I. Nanoparticles in thermotropic and lyotropic liquid crystals. *Front. Soft Matter.* **4**, 1518796. <https://doi.org/10.3389/fsm.2024.1518796> (2025).
22. Sharma, A., Malik, P., Dhar, R. & Kumar, P. Improvement in electro-optical and dielectric characteristics of ZnO nanoparticles dispersed in a nematic liquid crystal mixture. *Bull. Mater. Sci.* **42**, 215. <https://doi.org/10.1007/s12034-019-1902-5> (2019).
23. Ostrikov, K. *Plasma nanoscience, Basic Concepts and Application of Deterministic Nanofabrication* (Wiley-VCH, 2008).
24. Neyts, E. C., Ostrikov, K., Sunkara, M. K. & Bogaerts, A. Plasma catalysis: synergistic effects at the nanoscale. *Chem. Rev.* **115**, 13408. <https://doi.org/10.1021/acs.chemrev.5b00362> (2015).
25. Kaushik, N. K. et al. Plasma and nanomaterials: fabrication and biomedical applications. *Nanomaterials* **9**, 98. <https://doi.org/10.3390/nano9010098> (2019).
26. Patinglag, L. et al. Non-thermal plasma-based inactivation of bacteria in water using a microfluidic reactor. *Water Res.* **201**, 117321. <https://doi.org/10.1016/j.watres.2021.117321> (2021).
27. Zou, X. et al. Plasma activated oil: fast production, reactivity, stability, and wound healing application. *Sci. Eng.* **5**, 1611. <https://doi.org/10.1021/acsbiomaterials.9b00125> (2019).
28. Sadigh, M., Sayyar, Z., Mohammadi, M. A. & Baharlounezhad, F. Controlling the drug delivery efficiency of chitosan-based systems through silver nanoparticles and oxygen plasma. *Int. J. Biol. Macromol.* **294**, 139407. <https://doi.org/10.1016/j.ijbiomac.2024.139407> (2025).
29. Fatima, A., Zazimal, F. & Homola, T. A review of plasma modification strategies of nanomaterial for wastewater treatment. *JWPE* **77**, 108350. <https://doi.org/10.1016/j.jwpe.2025.108350> (2025).
30. Prost, J. & Gennes, P. G. *The Physics of Liquid Crystals* 2nd edn (Oxford University Press, 1993).
31. Najjar, R., Awad, R. & Abdel-Gaber, A. M. Physical properties of Mn<sub>2</sub>O<sub>3</sub> nanoparticles synthesized by co-precipitation method at different pH values. *J. Supercond. Nov. Magn.* <https://doi.org/10.1007/s10948-018-4765-x> (2018).
32. Farhood, S. T. et al. Green synthesis and characterization of  $\alpha$ -Mn<sub>2</sub>O<sub>3</sub> nanoparticles for antibacterial activity and efficient visible-light photocatalysis. *Sci. Rep.* **14**, 6755. <https://doi.org/10.1038/s41598-024-56666-2> (2024).
33. Sharrouf, M., Awad, R., Roumie, M. & Marhaba, S. Structural, optical and room temperature magnetic study of Mn<sub>2</sub>O<sub>3</sub> nanoparticles. *Mater. Sci. Appl.* **6**, 850–859. <https://doi.org/10.4236/msa.2015.610087> (2015).
34. Suryanarayana, C. & Norton, M. G. Practical aspects of X-ray diffraction. In: *X-ray Diffraction: A Practical Approach* (63–94). Boston, MA: Springer US. [https://doi.org/10.1007/978-1-4899-0148-4\\_3](https://doi.org/10.1007/978-1-4899-0148-4_3) (1998).
35. Bras, A. R., Dioniso, M., Huth, H., Schick, C. & Schonhals, A. Origin of glassy dynamics in liquid crystal studied by broadband dielectric and specific heat spectroscopy. *Phys. Rev. E* **75**, 061708. <https://doi.org/10.1103/PhysRevE.75.061708> (2007).
36. N.Dalir, S., Javadian, J., Kakemam, A. & Yousefi Evolution of electro-chemical and electro-optical properties of nematic liquid crystal doped with graphene oxide. *J. Mol. Liq.* **25**, 398–407. <https://doi.org/10.1016/j.molliq.2018.05.138> (2018).
37. Dhar, R. Comments of the fitting of Cole-Cole/Havriliak-Negami equation with the dielectric data under the influence of parasitic effects in order to exact correct parameters of the materials. *Mol. Liq.* **3343**, 117682. <https://doi.org/10.1016/j.molliq.2021.117682> (2021).
38. Yadan, N. & Dhar, R. Impedance Spectroscopy, In: D. K. Singh, M. Pradhan, A. Materny (eds) *Modern Techniques of spectroscopy. Progress in optical science and photonics*, Vol. 13, Springer, Singapore. [https://doi.org/10.1007/978-981-33-6084-6\\_19](https://doi.org/10.1007/978-981-33-6084-6_19).

## Author contributions

All authors contributed to the study conception and design. Sample preparation was performed by M. A. Mohammadi and F. Baharlounezhad. Experimental analysis was performed by M. Khadem Sadigh. The first draft of the manuscript was written by M. Khadem Sadigh. Writing – review & editing of manuscript was performed by M. Khadem Sadigh and A. Ranjkesh. All authors read and approved the final manuscript.

## Declarations

### Competing interests

The authors declare no competing interests.

### Additional information

**Correspondence** and requests for materials should be addressed to M.K.S.

**Reprints and permissions information** is available at [www.nature.com/reprints](http://www.nature.com/reprints).

**Publisher's note** Springer Nature remains neutral with regard to jurisdictional claims in published maps and institutional affiliations.

**Open Access** This article is licensed under a Creative Commons Attribution-NonCommercial-NoDerivatives 4.0 International License, which permits any non-commercial use, sharing, distribution and reproduction in any medium or format, as long as you give appropriate credit to the original author(s) and the source, provide a link to the Creative Commons licence, and indicate if you modified the licensed material. You do not have permission under this licence to share adapted material derived from this article or parts of it. The images or other third party material in this article are included in the article's Creative Commons licence, unless indicated otherwise in a credit line to the material. If material is not included in the article's Creative Commons licence and your intended use is not permitted by statutory regulation or exceeds the permitted use, you will need to obtain permission directly from the copyright holder. To view a copy of this licence, visit <http://creativecommons.org/licenses/by-nc-nd/4.0/>.

© The Author(s) 2025